Constructing Reliable Parametric Images Using Enhanced GLLS for Dynamic SPECT

Lingfeng Wen*, *Member, IEEE*, Stefan Eberl, *Member, IEEE*, Michael J. Fulham,
(David) Dagan Feng, *Fellow, IEEE*, and Jing Bai, *Fellow, IEEE*

***Abstract*—The generalized linear least square (GLLS) method can successfully construct unbiased parametric images from dynamic positron emission tomography data. Quantitative dynamic single photon emission computed tomography (SPECT) also has the potential to generate physiological parametric images. However, the high level of noise, intrinsic in SPECT, can give rise to unsuccessful voxelwise fitting using GLLS, resulting in physiologically meaningless estimates. In this paper, we systematically investigated the applicability of our recently proposed approaches to improve the reliability of GLLS to parametric image generation from noisy dynamic SPECT data. The proposed approaches include use of a prior estimate of distribution volume (V_d), a bootstrap Monte Carlo (BMC) resampling technique, as well as a combination of both techniques. Full Monte Carlo simulations were performed to generate dynamic projection data, which were then reconstructed with and without resolution recovery, before generating parametric images with the proposed methods. Four experimental clinical datasets were also included in the analysis. The GLLS methods incorporating BMC resampling could successfully and reliably generate parametric images. For high signal-to-noise ratio (SNR) imaging data, the BMC-aided GLLS provided the best estimates of K_1, while the BMC-V_d-aided GLLS proved superior for estimating V_d. The improvement in reliability gained with BMC-aided GLLS in low SNR image data came at the expense of some overestimation of V_d and increased computation time.**

***Index Terms*—Least square methods, parameter estimation, simulation, single photon emission computed tomography (SPECT).**

I. Introduction

POSITRON emission tomography (PET) and single photon emission computed tomography (SPECT) can noninvasively provide information about physiological and biochemical function at the molecular level by following the kinetics of radiotracers. Compartmental modeling of the kinetics of the radiotracers enables estimation of quantitative measures of the functional parameters relevant to metabolic, physiological, and biochemical processes. For traditional kinetic analysis, tissue time activity curves (TTACs) are derived from regions of interest (ROIs) placed on the dynamic images and the input function (IF) is obtained from blood or plasma samples. Compartment model parameters describing the TTAC's kinetics for the given IF are then typically estimated with nonlinear least square (NLS) fitting to provide the functional parameters of interest [1]. Rather than manually placing ROIs on only selected regions in the images, which is subjective and can be time consuming, it is attractive to fit the compartment model to TTACs derived for each voxel to generate parametric images for the whole image volume.

The computational burden of NLS and intolerance to the high level of noise in voxel-derived TTACs make NLS largely unsuitable for parametric image generation from SPECT and PET data. Graphical plot methods, such as the Patlak and Logan plots, transform the nonlinear compartment model solution equations into linear plots, allowing direct derivation of limited, specific parameters from linear regression analysis [2], [3]. However, the graphical plots provide only a limited number of parameters, typically no more than two. The underlying assumptions may give rise to bias in the parametric images derived by the graphical plots. The linear least squares (LLS) method tackles the parameter estimation by setting up and solving matrices of linear equations through integrations of the IF and TTACs. However, measurement errors from multiple measurements or frames contribute to each of the integrals, so the measurement errors of the linearized equation terms are no longer independent that can lead to bias in the parameters estimated by the LLS method.

The generalized LLS (GLLS) method was proposed to address this shortcoming of the LLS method and to provide unbiased estimation [4], [5]. While the GLLS method has been successfully applied to PET data in the brain, heart, and liver [5]–[7], the high level of noise intrinsic in SPECT data can give rise to physiologically meaningless fits when GLLS is applied to voxelwise SPECT data TTACs, resulting in physiologically meaningless estimates such as negative or unrealistically high kinetic constants. The noise in the image can potentially be reduced by spatial low-pass filtering. However, low-pass filtering

Manuscript received April 7, 2008; revised June 27, 2008, August 23, 2008, and October 23, 2008. First published December 9, 2008; current version published May 6, 2009. This study was supported in part by the Australian Research Council (ARC), the Hong Kong Polytechnic University (PolyU), the National Natural Science Foundation of China (NSFC) grants, and in part by the Australia–China special fund of the Australian International Science Linkage. *Asterisk indicates corresponding author.*

*L.Wen is with the Department of PET and Nuclear Medicine, Royal Prince Alfred Hospital, Sydney, NSW 2050, Australia, and also with the Biomedical and Multimedia Information Technology Research Group, the School of Information Technologies, University of Sydney, Sydney, NSW 2006, Australia. He is also with the Department of Electronic and Information Engineering, Hong Kong Polytechnic University, Kowloon, Hong Kong (e-mail: wenlf@ieee.org).

S. Eberl and M. J. Fulham are with the Department of PET and Nuclear Medicine, Royal Prince Alfred Hospital, Sydney, NSW 2050, Australia, and also with the Biomedical and Multimedia Information Technology Research Group, the School of Information Technologies, University of Sydney, NSW 2006, Australia.

D. Feng is with the Biomedical and Multimedia Information Technology Research Group, the School of Information Technologies, University of Sydney, Sydney, NSW 2006, Australia, also with the Department of Electronic and Information Engineering, Hong Kong Polytechnic University, Kowloon, Hong Kong. He is also with the Med-X Research Institute, Shanghai Jiao Tong University, Shanghai 200030, China.

J. Bai is with the Department of Biomedical Engineering, Tsinghua University, 100084 Beijing, China.

Digital Object Identifier 10.1109/TBME.2008.2009998

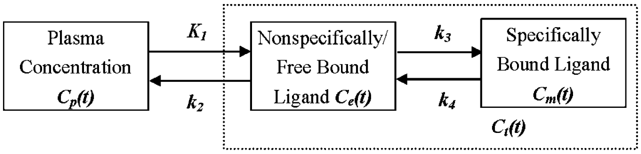

Fig. 1. Three-compartment and four-parameter kinetic model for the neuroreceptor study.

further increases the already pronounced partial volume effect (PVE) in SPECT data leading to increased bias. In addition, based on our previous work, it does not necessarily improve the reliability of the fits [8].

The focus of this study has thus been to develop and evaluate robust, GLLS-based, parametric imaging techniques for noisy SPECT data without undue reliance on heavy spatial filtering. Recently, we proposed three approaches for enhancing GLLS using prior information and a statistical resampling technique [9]. The first method incorporates a prior volume of distribution (V_{d}) estimate in the GLLS fitting to reduce the parameter space (V_{d}-aided GLLS). The second method utilizes bootstrap Monte Carlo (BMC) statistical resampling to reject physiologically meaningless fits (BMC-aided GLLS). The third method combines statistical resampling and the prior estimate of V_{d} (BMC-V_{d}-aided GLLS). In our previous investigation [9], the statistical resampling techniques were able to improve the reliability of parameter estimation. However, this investigation was largely limited to simulated TTACs with Gaussian noise model, which, while representative of TTACs from ROI analysis, do not necessarily completely reflect the characteristics, noise distributions, and correlations in the voxel-by-voxel TTACs caused by the imaging and reconstruction processes.

Thus, in this study, to accurately reflect these processes, Monte Carlo simulations incorporating a realistic model of the imaging processes were used to generate dynamic projection data. These were then reconstructed similar to clinical dynamic SPECT studies performed on the triple head gamma camera at the Royal Price Alfred Hospital. These realistic, simulated dynamic SPECT data as well as experimentally acquired dynamic SPECT data form the basis of this study to evaluate and optimize the proposed enhanced GLLS methods for generating parametric images from dynamic SPECT data. Bias, computational burden, and reliability of estimating voxel-by-voxel parameters at a range of noise levels typically encountered in dynamic SPECT studies were used to draw conclusions of the relative merits of the approaches under consideration.

II. METHODS

A. GLLS Method

To demonstrate the theory of the GLLS and advanced methods, a three-compartment and four-parameter kinetic model for the neuroreceptor study shown in Fig. 1 was assumed. $C_p(t)$ is the radiotracer concentration in the plasma over time, $C_e(t)$ is the concentration of free and nonspecifically bound radioligand in the tissue, and $C_m(t)$ is the concentration of specifically bound radioligand in the tissue. K_1, k_2, k_3, and k_4 are rate constants connecting adjacent compartments in Fig. 1.

Molecular imaging measures the total radioligand activity concentration $C_i(t), = C_e(t) + C_m(t)$, in the tissue, which can be presented in the form of the differential equation

$$\frac{d^2C_i(t)}{dt^2} = K_1\frac{dC_p(t)}{dt} + K_1(k_3+k_4)C_p(t) - (k_2+k_3+k_4)\frac{dC_i(t)}{dt} - k_2k_4C_i(t). \quad (1)$$

By substituting $P_1 = K_1, P_2 = K_1(k_3+k_4), P_3 = -(k_2 + k_3 + k_4), P_4 = -k_2k_4$, and by taking Laplace transforms, equation (1) can be rearranged to (2) when the measurement of TTAC is assumed to be equal to the true value of $C_i(t)$ plus an independent, Gaussian-distributed noise term $e(t)$

$$C_i(s) = \frac{sP_1C_p(s) + P_2C_p(s)}{s^2 - sP_3 - P_4} + E(s). \quad (2)$$

The term $E(s)$ represents the white measurement noise of the TTAC. Equation (2) can then be rewritten into

$$s^2C_i(s) = sP_1C_p(s) + P_2C_p(s) + sP_3C_i(s) + P_4C_i(s) + (s^2 - sP_3 - P_4)E(s). \quad (3)$$

Equation (3) depicts the noise term colored by the term $s^2 - sP_3 - P_4$, even if the measurement noise $E(s)$ is white. This colored noise term can lead to bias in the estimates. The principle of the GLLS method is to prewhiten the colored noise term by using an autoregressive filter $F(s) = s^2 - s\hat{P}_3 - \hat{P}_4$, where $\hat{P}_1$, $\hat{P}_2$, $\hat{P}_3$, and $\hat{P}_4$ are estimates of P_1, P_2, P_3, and P_4, shown as

$$\frac{s^2C_i(s)}{s^2 - s\hat{P}_3 - \hat{P}_4} = \frac{sP_1C_p(s)}{s^2 - s\hat{P}_3 - \hat{P}_4} + \frac{P_2C_p(s)}{s^2 - s\hat{P}_3 - \hat{P}_4} + \frac{sP_3C_i(s)}{s^2 - s\hat{P}_3 - \hat{P}_4} + \frac{P_4C_i(s)}{s^2 - s\hat{P}_3 - \hat{P}_4} + \frac{(s^2 - sP_3 - P_4)}{s^2 - s\hat{P}_3 - \hat{P}_4}E(s). \quad (4)$$

If $F(s)$ approximates the term $s^2 - sP_3 - P_4$, the noise in (4) is whitened and the estimates would become unbiased. In this case, equation (4) can be transformed back into the temporal domain by the inverse Laplace transform with the noise term neglected, shown as

$$C_i(t) + \hat{P}_3\psi_1 \otimes C_i(t) + \hat{P}_4\psi_2 \otimes C_i(t) = \hat{P}_1\psi_1 \otimes C_p(t) + \hat{P}_2\psi_2 \otimes C_p(t) + \hat{P}_3\psi_1 \otimes C_i(t) + \hat{P}_4\psi_2 \otimes C_i(t) \quad (5)$$

where $\otimes$ is the mathematical convolution operator, $\psi_1 = (\lambda_2\, e^{-\lambda_2 t} - \lambda_1\, e^{-\lambda_1 t})/(\lambda_2 - \lambda_1)$, and $\psi_2 = (e^{-\lambda_1 t} - e^{-\lambda_2 t})/(\lambda_2 - \lambda_1)$. The values of λ_1 and λ_2 are determined by $\hat{P}_3$ and $\hat{P}_4$ with $\lambda_1 = -(\hat{P}_3 + \sqrt{\hat{P}_3 + 4\hat{P}_4})/2$ and $\lambda_2 = -(\hat{P}_3 - \sqrt{\hat{P}_3 + 4\hat{P}_4})/2$.

In terms of n-frame imaging protocol, $S = [t_1, t_2, \ldots, t_n]$ for the TTAC with t_i representing the middle time of the sampling interval, the estimates of the GLLS method can be solved in the matrix form in (6) by deriving the estimates $\hat{\theta}_{\mathrm{GLLS}} = [\hat{P}_1, \hat{P}_2,$

$\hat{P}_3, \hat{P}_4]^T$

$$\hat{\theta}_{\mathrm{GLLS}} = (Z^T Z)^{-1} Z^T r \tag{6}$$

where

$$r = \begin{bmatrix} C_i(t_1) + \hat{P}_3\psi_1 \otimes C_i(t_1) + \hat{P}_4\psi_2 \otimes C_i(t_1) \\ C_i(t_2) + \hat{P}_3\psi_1 \otimes C_i(t_2) + \hat{P}_4\psi_2 \otimes C_i(t_2) \\ \vdots \\ C_i(t_n) + \hat{P}_3\psi_1 \otimes C_i(t_n) + \hat{P}_4\psi_2 \otimes C_i(t_n) \end{bmatrix}$$

$$Z = \begin{bmatrix} \psi_1 \otimes C_p(t_1), \psi_2 \otimes C_p(t_1), \psi_1 \otimes C_i(t_1), \psi_2 \otimes C_i(t_1) \\ \psi_1 \otimes C_p(t_2), \psi_2 \otimes C_p(t_2), \psi_1 \otimes C_i(t_2), \psi_2 \otimes C_i(t_2) \\ \vdots \\ \psi_1 \otimes C_p(t_n), \psi_2 \otimes C_p(t_n), \psi_1 \otimes C_i(t_n), \psi_2 \otimes C_i(t_n) \end{bmatrix}.$$

The estimates of rate constant ($\hat{K}_1, \hat{k}_2, \hat{k}_3$, and $\hat{k}_4$) for the model shown in Fig. 1 can then be derived according to

$$\hat{K}_1 = \hat{P}_1, \qquad \hat{k}_2 = -\frac{\hat{P}_2}{\hat{P}_1} - \hat{P}_3, \qquad \hat{k}_3 = -\hat{P}_3 - \hat{k}_2 - \hat{k}_4,$$
$$\hat{k}_4 = -\frac{\hat{P}_4}{\hat{k}_2}. \tag{7}$$

Iterations are required for the GLLS method to update the estimated parameters for the autoregressive filter *F*(*s*). Estimates of $\hat{P}_1, \hat{P}_2, \hat{P}_3$, and $\hat{P}_4$ from the previous iteration are used in (6) to obtain an improved estimate of the parameters, P_1, P_2, P_3, and P_4, for the current iteration. Initial estimates for these parameters are obtained from LLS fitting. Iterations are continued until the termination criteria are reached [10]. In practice, two or three iterations have been found to provide satisfactory results for PET data.

B. V_{d}-*Aided GLLS*

Despite the introduction of the autoregressive filter, the original GLLS method does not always cope with the high noise in SPECT data, which results in meaningless estimates. The volume of distribution V_{d}, which reflects the equilibrium distribution of the tracer in the tissue, is relatively stable in contrast to other kinetic constants. If a prior V_{d} is known, the reduction in the parametric domain and in the number of estimated parameters should result in enhanced parameter estimation reliability.

For the three-compartment and four-parameter kinetic model in Fig. 1, the volume of distribution can be represented by the ratio of P_2 and P_4 in

$$V_{\mathrm{d}} = \frac{K_1}{K_2}\left(1 + \frac{k_3}{k_4}\right) = -\frac{P_2}{P_4}. \tag{8}$$

Equation (1) can be organized into (9) with P_2 substituted by the expression of V_{d} and P_4

$$\frac{d^2}{dt^2}C_i(t) = P_1\frac{d}{dt}C_p(t) + P_3\frac{d}{dt}C_i(t) + P_4[C_i(t) - V_{\mathrm{d}}C_p(t)]. \tag{9}$$

The corresponding matrix solution for the V_{d}-aided GLLS is then given by (10) with $\hat{\theta}_{V_{\mathrm{d}}\text{-GLLS}} = [\hat{P}_1, \hat{P}_3, \hat{P}_4]^T$

$$\hat{\theta}_{V_{\mathrm{d}}\text{-GLLS}} = (Z_{V_{\mathrm{d}}}^T Z_{V_{\mathrm{d}}})^{-1} Z_{V_{\mathrm{d}}}^T \cdot r \tag{10}$$

where

$$Z_{V_{\mathrm{d}}} = \begin{bmatrix} \psi_1 \otimes C_p(t_1), \psi_1 \otimes C_i(t_1), \psi_2 \otimes C_i(t_1) - V_{\mathrm{d}}\psi_2 \otimes C_p(t_1) \\ \psi_1 \otimes C_p(t_2), \psi_1 \otimes C_i(t_2), \psi_2 \otimes C_i(t_2) - V_{\mathrm{d}}\psi_2 \otimes C_p(t_2) \\ \vdots \\ \psi_1 \otimes C_p(t_n), \psi_1 \otimes C_i(t_n), \psi_2 \otimes C_i(t_n) - V_{\mathrm{d}}\psi_2 \otimes C_p(t_n) \end{bmatrix}.$$

The prior estimate of V_{d} can be derived from the GLLS method for two-compartment and two-parameter model [11], which may be biased due to the difference between the underlying models. In this case, the optimal V_{d} would need to be found by performing the GLLS fit for a range of V_{d} values around the prior V_{d} estimate. To simplify the assessment of the V_{d}-aided GLLS performance, the Logan plot, with the same underlying three-compartment and four-parameter model was used to derive the prior V_{d} in this study.

C. *BMC-Aided GLLS*

The BMC technique is a well-established robust resampling method that allows multiple synthetic datasets to be derived from a measured set without any assumptions about the noise model and noise level [12]. It only requires that the sequential order of the data points does not matter in the data processing. Thus, BMC allows multiple synthetic curves to be generated for each TTAC. GLLS is then applied to these synthetic curves—some of the fits are meaningless and others yield meaningful results and are retained. Thus, successful fits can be obtained even for TTACs for which the original GLLS fit was physiologically meaningless.

To generate synthetic, new estimates of the true TTAC, the BMC technique is applied to randomly drawn *m* samples for a given curve of *m* data points. Some points will be duplicated while others are not selected. For example, for a ten-point curve: $\{(t_1, C_{t1}), (t_2, C_{t2}), \ldots, (t_9, C_{t9}), (t_{10,} C_{t10})\}$, the random resampling procedure generates one instance of the synthetic curves, $\{(t_3, C_{t3}), (t_6, C_{t6}), (t_2, C_{t2}), (t_7, C_{t7}), (t_3, C_{t3}), (t_8, C_{t8}), (t_4, C_{t4}), (t_{10}, C_{t10}), (t_6, C_{t6}), (t_5, C_{t5})\}$, with the duplication of the third and sixth points and the omission of the first and ninth points. Based on the assumption that the order does not matter, sorting the samples based on sampling time would derive a synthetic TTAC $\{(t_2, C_{t2}), (t_3, C_{t3}), (t_3, C_{t3}), (t_4, C_{t4}), (t_5, C_{t5})(t_6, C_{t6}), (t_6, C_{t6}), (t_7, C_{t7}), (t_8, C_{t8}), (t_{10}, C_{t10})\}$, which will be fitted by using GLLS.

The proposed BMC-aided GLLS derives a number of BMC curves for each voxelwise TTAC. Once ten fits are achieved with physiologically meaningful estimates, the BMC resampling is stopped and the mean parameters of the successful fits are used as the outcomes.

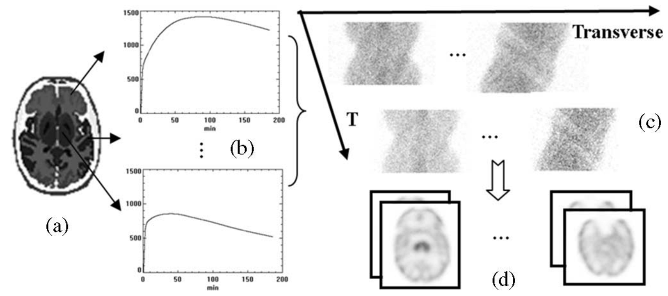

Fig. 2. Data flow of full Monte Carlo simulation. (a) Mathematical brain phantom. (b) Experimental kinetics. (c) Dynamic projection data. (d) Dynamic reconstruction data.

D. BMC-$V_{\rm d}$-Aided GLLS

Instead of using the original GLLS in the fitting for the BMC curves, the enhanced GLLS method using the constraint of a prior $V_{\rm d}$ can be also incorporated into the BMC technique for potential further improvement. The BMC-$V_{\rm d}$-aided GLLS method is quite similar to the BMC-aided GLLS method mentioned earlier with the fitting equation derived by the $V_{\rm d}$-aided GLLS (10). Again, the prior estimate of $V_{\rm d}$ is obtained by the Logan plot method.

As the computational burden is proportional to the number of generated BMC curves, the maximum number of BMC curves for both BMC-aided and BMC-$V_{\rm d}$-aided GLLS was set at 200 per voxel regardless of achieving ten meaningful fits to avoid excessively long running time in the investigation. Fits with any of rate constants $(K_1, k_2, k_3, \text{ and } k_4)$ less than 0 or higher than 1 were regarded to be physiologically meaningless.

E. Computer Simulation of Dynamic SPECT Data

Fig. 2 demonstrates the data flow of the computer simulation. High count static projection data for individual structures in the Zubal mathematical human brain phantom [13] [Fig. 2(a)] were simulated by the SimSET Monte Carlo package [14]. The collimator module specified a parallel hole collimator with an energy window of 20% centered around 159 keV for ^{123}I. A flat SPECT detector was assumed using a simple Gaussian energy blurring model with an energy resolution of 10% full-width at half-maximum (FWHM). Effects of photon attenuation and Compton scatter were included in the simulations as was the penetration of high-energy photons of ^{123}I through the low-energy high-resolution (LEHR) collimator septa. The simulation projection matrix was 128 × 85 matrix × 120 angles per frame. A total of 36 frames covered the time course of the dynamic study, and consisted of 15 1-min scans, nine 5-min scans, and 12 10-min scans.

Separate projection data were simulated for the individual brain structures [8], including all the grey matter and white matter structures identified in the Zubal phantom, for a total number of 500 million decays each. The dynamic projection data [Fig. 2(c)] were then generated according to the experimentally observed kinetics of the neuronal nicotinic acetylcholine receptor tracer 5-[^{123}I]-iodo-A-85380 [15] [Fig. 2(b)], for five different levels of Poisson noise to cover the range of noise observed in experimental studies. In addition, an essentially noise-free set of projections was also simulated to act as reference for determining the impact of noise.

F. Reconstruction

The dynamic projection datasets were scatter corrected by the transmission-dependent scatter correction method [16] and septal penetration of the high-energy photons of ^{123}I was corrected by adding a constant background term to the scatter correction [17]. The scatter corrected dynamic projection data were reconstructed with the ordered-subset expectation-maximization (OS-EM) iterative reconstruction method [18] using 20 subsets and two iterations without resolution recovery [Fig. 2(d)]. Attenuation correction was included in the OS-EM reconstruction using an attenuation coefficient map for ^{123}I derived from the mathematical phantom.

Resolution recovery potentially improves quantitative accuracy by reducing PVE. It can be achieved in the reconstruction by modeling the resolution degrading factors. Thus, the OS-EM reconstructions were also performed with attenuation correction and resolution recovery. The parameters for the resolution recovery were based on the resolution model used in the Monte Carlo simulations. To account for the slower convergence when resolution recovery is included in the reconstruction, 40 subsets and 20 iterations were used.

G. Kinetic Analysis and Evaluation

Voxelwise parameter estimates of K_1, k_2, k_3, and k_4 were derived with each of the methods under investigation. Parametric images of $V_{\rm d}$ were then derived from the rate constant estimates (8) for the three-compartment and four-parameter model shown in Fig. 1. Volumes of interests (VOIs) were defined for the thalamus, cerebellum, and frontal cortex from the Zubal human brain phantom. A total of 20 sets of dynamic data were simulated for each level of noise to allow the evaluation of accuracy and reliability of the estimates.

Percentage bias for each VOI was calculated according to (11) for K_1 and $V_{\rm d}$. Coefficient of variation (CV) across the 20 simulation datasets was derived with (12) to compare the reliability of the estimates, as shown (11) and (12), at the bottom of the next page.

In (11) and (12), $p_{i,j}$ is the estimated parameter for the *j*th voxel in the VOI for the *i*th simulation dataset, p_0 is the known parameter value used in the generation of dynamic projection data. *M* is the number of simulation datasets for each noise levels, i.e., 20 in this study and *N* is the total number of voxels for the selected VOI (248 voxels for thalamus, 1458 voxels for cerebellum, and 2250 voxels for frontal cortex).

Estimated mean square error (EMSE), the sum of squared bias and variance for parameter estimates, as shown in (13), was used to evaluate the best compromise between the accuracy and reliability in constructing parametric images by the studied methods. For a given dataset, VOI and noise level, the method with the minimum EMSE receives a score of 1, while the other methods receive a score of 0 for the particular dataset and region. The scores for all datasets (different noise levels and VOIs) were then summed to derive an overall score

$$\mathrm{EMSE} = \left[\frac{1}{M}\left(\sum_{i=1}^{M}\sum_{j=1}^{N}\frac{p_{i,j}}{N}\right) - p_o\right]^2 + \frac{1}{M-1}\left[\sum_{i=1}^{M}\left(\sum_{j=1}^{N}\frac{p_{i,j}}{N}\right)^2 - M\left(\sum_{i=1}^{M}\sum_{j=1}^{N}\frac{p_{i,j}}{N}\right)^2\right]. \quad (13)$$

H. Animal Studies Analysis

The investigated methods were also applied to derive the parametric images from dynamic SPECT studies acquired in baboons with the neuronal nicotinic acetylcholine receptor tracer 5-[^{123}I]-iodo-A-85380 on a Triad XLT triple head gamma camera (Trionix Research Laboratories, Twinsburg, OH) [15]. Four dynamic studies were acquired in two adult *Papio hamadryas* baboons. The studies were approved by the Central Sydney Area Health Service Animal Welfare Committee. Dynamic SPECT scans were performed at the start of a 2-min infusion of 397 ± 43 MBq of 5-[^{123}I]-iodo-A-85380 for a total of 3-h acquisition time with the same sampling schedule as that detailed in the computer simulation. Transmission maps collected prior to the emission scan were used to achieve scatter-corrected emission data (128 × 64 matrix × 60 angles per frame) [16], and transmission-based attenuation correction using the OS-EM method [18] with 20 subsets of two iterations.

The experimental reconstruction data were processed similar to the simulation data. Manually defined ROIs were then applied to the constructed parametric images to yield estimated parameters for comparison.

III. RESULTS

A. No Resolution Recovery

Fig. 3 shows the plots of the percentage bias of K_1 and V_d for the frontal cortex in the simulation data. The V_d-aided GLLS suffered from the highest negative bias, worse than the original GLLS. The results showed meaningless fits for most image voxels for the V_d-aided GLLS, which resulted in almost -100% biases of K_1 and V_d, as voxels with meaningless fits were set to zero in the parametric images. The results also showed the BMC-aided and BMC-V_d-aided GLLS methods substantially reduced the bias by avoiding meaningless fits as compared with the original GLLS. Compared with the results without noise added (noise level 0 in Fig. 3), K_1 was underestimated by the BMC-aided and BMC-V_d-aided GLLS. V_d was also underestimated by the BMC-V_d-aided GLLS, but overestimated by the BMC-aided GLLS.

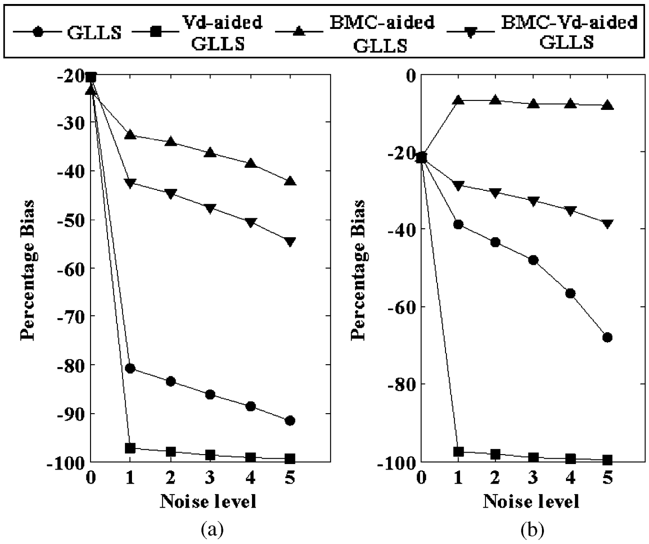

(a) (b)

Fig. 3. Percentage bias as a function of increasing noise level for the frontal cortex without resolution recovery. (a) K_1. (b) V_d (0 represents noiseless data, 5 represents the highest noise level).

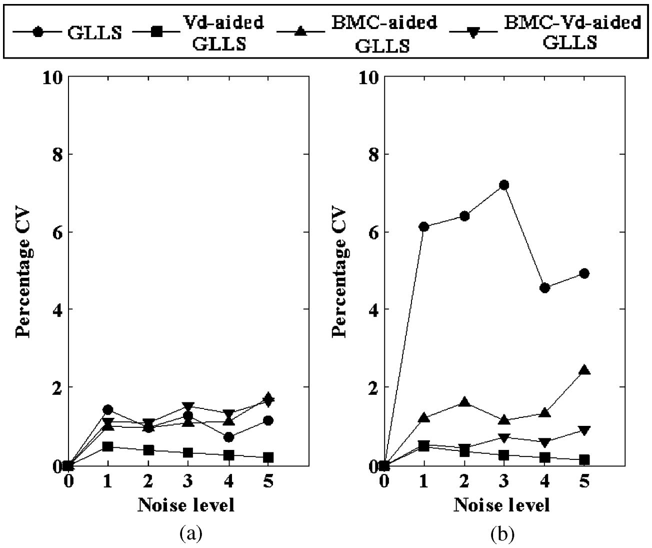

(a) (b)

Fig. 4. Percentage CV as a function of increasing noise level for the frontal cortex without resolution recovery. (a) K_1. (b) V_d.

Fig. 4 shows the plots of the CVs of parameter estimates K_1 and V_d for the frontal cortex in the simulation data. The CV for

---

$$\mathrm{Bias} = \frac{1}{M}\frac{\left[\sum_{i=1}^{M}\sum_{j=1}^{N}(p_{i,j}-p_o)/N\right]}{P_o} \times 100\% \quad (11)$$

$$\mathrm{CV} = \frac{\left[\sqrt{\left(\sum_{i=1}^{M}\left(\sum_{j=1}^{N}p_{i,j}/N\right)^2 - M\left(\sum_{i=1}^{M}\sum_{j=1}^{N}p_{i,j}/N\right)^2\right)/(M-1)}\right]}{p_o} \times 100\% \quad (12)$$

TABLE I
PERCENTAGE BIAS (PERCENTAGE CV) FOR ESTIMATED PARAMETER AT MODERATE NOISE LEVEL WITHOUT RESOLUTION RECOVERY

	Cerebellum	Thalamus	Frontal cortex
K_1 for GLLS	-68.8 (2.0)	-90.1 (2.4)	-86.2 (1.3)
K_1 for VGLLS [a]	-93.9 (1.0)	-99.7 (0.3)	-98.6 (0.3)
K_1 for BGLLS [b]	-9.6 (1.3)	-29.5 (4.7)	-36.3 (1.1)
K_1 for BVGLLS [c]	-19.0 (1.4)	-44.1 (3.7)	-47.5 (1.5)
V_d for GLLS	-13.8 (11.2)	-55.5 (12.5)	-47.9 (7.2)
V_d for VGLLS [a]	-94.0 (0.9)	-99.8 (0.3)	-98.8 (0.3)
V_d for BGLLS [b]	21.5 (2.3)	24.3 (5.6)	-7.7 (1.1)
V_d for BVGLLS [c]	-3.4 (0.7)	-27.2 (1.6)	-32.7 (0.7)

[a] VGLLS: V_d-aided GLLS; [b] BGLLS: BMC-aided GLLS; [c] BVGLLS: BMC-V_d-aided GLLS.

most methods was low (<2.5%), with the exception of the CV of V_d by the original GLLS, which reached nearly 8%.

Similar results were also observed in the thalamus and cerebellum, as shown in Table I, which summarizes percentage bias and CVs by the studied methods for simulation data at a moderate noise level (noise level 3 in Figs. 3 and 4). Around -100% biases of K_1 and V_d were observed also for the cerebellum and thalamus for the V_d-aided GLLS method. Thus, the simple incorporation of prior V_d into GLLS fitting further degraded the performance for noisy SPECT data, with the degradation being substantially more pronounced than that observed in our previous investigation with simulated TTACs [9].

As no correction for PVEs was applied, underestimation with negative bias was expected due to marked PVE in SPECT data. However, positive bias of V_d was observed for the thalamus and cerebellum by the BMC-aided GLLS. Thus, if PVE correction had been applied to the data, the observed overestimation of V_d for the BMC-aided GLLS would have likely even been more pronounced. It was interesting to observe less bias of K_1 achieved by the BMC-aided GLLS compared to the results of the BMC-V_d-aided GLLS (reduction in bias ranged from 9.4% in the cerebellum to 14.6% in the thalamus) while V_d was overestimated by the BMC-aided GLLS (Table I).

B. Resolution Recovery

Fig. 5 shows the plots of the percentage bias of K_1 and V_d for the frontal cortex when resolution recovery was included in the reconstruction for the simulation data. Resolution recovery virtually eliminated PVE for the noiseless data (noise level 0) and reduced the bias correspondingly for noisy data. The overestimation and reduction of bias for V_d seen with the BMC-aided GLLS for noisy data without resolution recovery, now results in a positive bias [Fig. 5(b)]. The CVs for the two methods with Bootstrap resampling technique were less than 1.5%, while the CVs for the original GLLS reached 3.5% for K_1 and 6.5% for V_d.

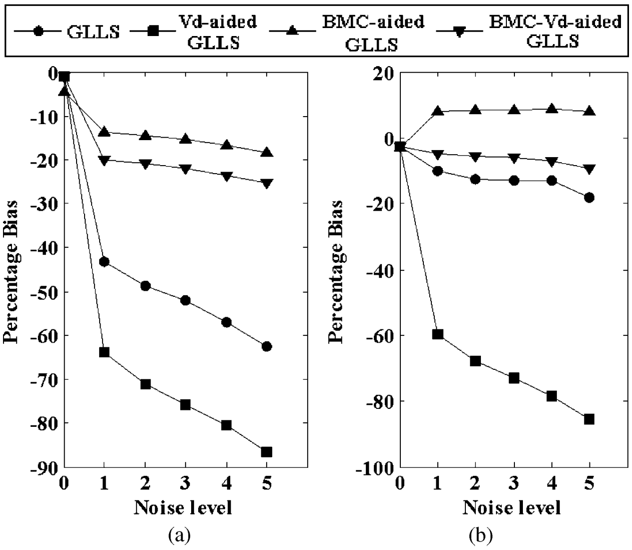

(a) (b)

Fig. 5. Percentage bias as a function of increasing noise level for the frontal cortex with resolution recovery. (a) K_1. (b) V_d.

TABLE II
PERCENTAGE BIAS (PERCENTAGE CV) FOR ESTIMATED PARAMETER AT MODERATE NOISE LEVEL WITH RESOLUTION RECOVERY

	Cerebellum	Thalamus	Frontal cortex
K_1 for GLLS	-18.0 (4.9)	-70.9 (11.4)	-52.0 (2.1)
K_1 for VGLLS [a]	-37.3 (6.1)	-92.3 (4.4)	-75.7 (2.2)
K_1 for BGLLS [b]	4.6 (1.9)	-6.6 (6.4)	-15.3 (0.9)
K_1 for BVGLLS [c]	-2.4 (1.8)	-10.6 (4.1)	-21.9 (0.8)
V_d for GLLS	16.0 (9.3)	-18.1 (30.8)	-12.8 (6.1)
V_d for VGLLS [a]	-31.4 (6.3)	-89.7 (6.2)	-73.0 (2.2)
V_d for BGLLS [b]	25.9 (0.8)	60.9 (7.4)	8.5 (0.6)
V_d for BVGLLS [c]	12.3 (0.4)	29.6 (3.3)	-6.1 (0.3)

[a] VGLLS: V_d-aided GLLS; [b] BGLLS: BMC-aided GLLS; [c] BVGLLS: BMC-V_d-aided GLLS.

TABLE III
EVALUATIVE SCORES BASED ON MINIMUM VALUES OF EMSE

	NRR [a]		WRR [b]	
	K_1	V_d	K_1	V_d
GLLS	0	0	0	1
V_d-aided GLLS	0	0	0	0
BMC-aided GLLS	15	9	11	1
BMC-V_d-aided GLLS	0	6	4	13

[a] NRR: without resolution recovery; [b] WRR: with resolution recovery.

Similar trends were also observed in the thalamus and cerebellum. The results of K_1 and V_d are summarized in Table II for the resolution-recovered simulation data at a moderate noise level. The resolution-recovery-based PVE correction led to a more pronounced overestimation of V_d by the BMC-aided GLLS, especially, in the thalamus (exceeding 60%). The BMC-V_d-aided GLLS also achieved positive bias of V_d, which is mainly attributed to the suboptimal resolution recovery, giving rise to overcompensation for some specific regions.

Table III lists the evaluation scores of EMSE for K_1 and V_d for the simulation data without and with resolution recovery. For the resolution recovery reconstructions, the BMC-aided GLLS provided better estimates of K_1, while better estimates of V_d were achieved by the BMC-V_d-aided GLLS. For the simulation data without PVE correction, the overestimation of V_d by the BMC-aided GLLS partially compensated for the biased estimation of V_d, which resulted in the BMC-aided GLLS providing optimal estimates for both K_1 and V_d.

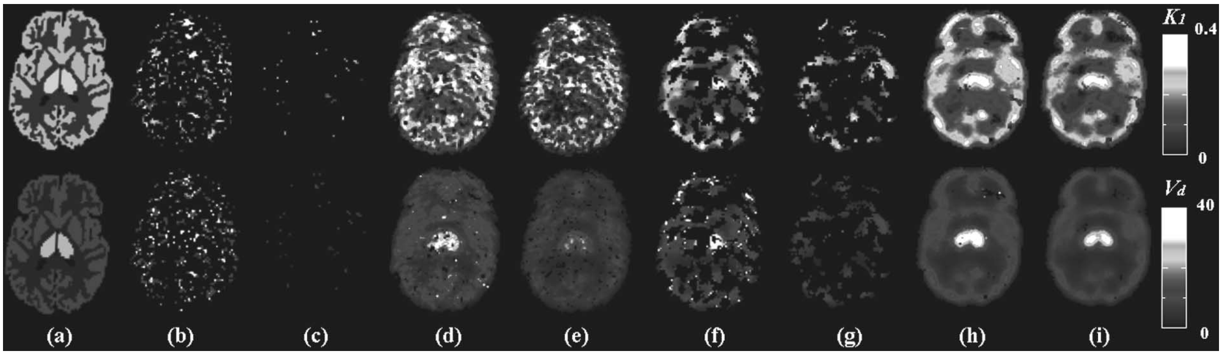

Fig. 6. Parametric images of K_1 and V_d for the simulated data at highest level of noise. (a) Original referenced images. (b) GLLS (without resolution recovery). (c) V_d-aided GLLS (without resolution recovery). (d) BMC-aided GLLS (without resolution recovery). (e) BMC-V_d-aided GLLS (without resolution recovery). (f) GLLS (with resolution recovery). (g) V_d-aided GLLS (with resolution recovery). (h) BMC-aided GLLS (with resolution recovery). (i) BMC-V_d-aided GLLS (with resolution recovery).

C. Parametric Images of Simulation Data

Fig. 6 depicts the derived parametric images of K_1 and V_d for the simulation data at the highest level of noise without and with resolution recovery. For the noisy SPECT data, the original GLLS suffered from a large number of physiologically meaningless fits [Fig. 6(b)], which resulted in the loss of detail in the parametric images even for the resolution-recovered simulation data [Fig. 6(f)]. The images by the V_d-aided GLLS method were largely blank due to almost all voxel fits being physiologically meaningless, and hence, being set to zero in the parametric images [Fig. 6(c) and (g)].

The BMC-aided GLLS and BMC-V_d-aided GLLS achieved similar parametric images of K_1 with slightly higher values of K_1 for the BMC-aided GLLS [top row, Fig. 6(d) and (h)]. However, the images of V_d differed between these two methods. The V_d values were generally higher for the BMC-aided GLLS method and the thalamus was thus more pronounced due to the overestimation in this region [bottom row, Fig. 6(d) and (h)]. The V_d images for BMC-aided GLLS also tended to be noisier than those derived by BMC-V_d-aided GLLS method [bottom row, Fig. 6(d) and (e)] for the simulation data without resolution recovery.

All parametric image simulations were performed on a SUN Blade-2000 workstation. Compared to the original GLLS computation time of 12.6 minutes per dynamic study, the average running times for the simulation data without (with) resolution recovery were 1.0 (1.1), 61.7 (27.0), and 83.2 (36.3) times higher for the V_d-aided, BMC-aided, BMC-V_d-aided GLLS methods, respectively. Thus, the improvement in the parametric images achieved with the BMC-aided methods came at the expense of increased computation time. In other words, more noisy functional imaging data require more computation time to construct parametric images using the GLLS methods with the BMC technique. This is in line with the results of computation time observed for the enhanced BMC-aided GLLS. For instance, for the simulation data with resolution recovery, the average running times by the BMC-V_d-aided GLLS were 29.2, 32.3, 36.0, 39.8, and 44.2 times those of original GLLS computation times for the noise levels increasing from 1 to 5, respectively. This is due to typically more BMC iterations required with increasing noise level to achieve ten successful fits.

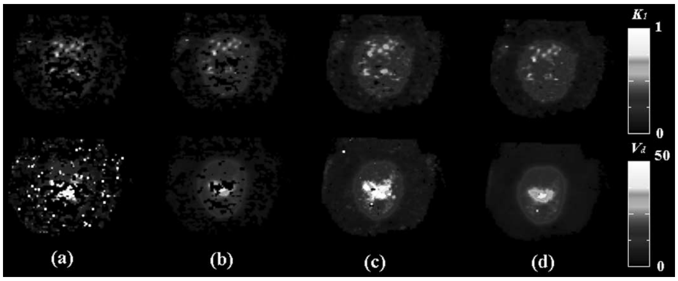

Fig. 7. Parametric images of K_1 and V_d for the experimental data derived by (a) GLLS; (b) V_d-aided GLLS; (c) BMC-aided GLLS; (d) BMC-V_d-aided GLLS.

D. Experimental Studies

Fig. 7 presents the parametric images of K_1 and V_d for one experimental dataset. The results were largely consistent with the simulation data findings. Contrary to the simulation findings, for these data, the V_d-aided GLLS seemed to improve the reliability and remove "outliers" compared with the original GLLS method. However, it still suffered from physiologically meaningless fits with a large number of "blank" voxels in the images. No marked differences were observed for K_1 between the two BMC-aided methods, while the BMC-V_d-aided GLLS achieved better parametric images for V_d by visual inspection.

Fig. 8 shows the plots of the mean values of K_1 and V_d for manually defined frontal cortex regions in the experimental studies. Two studies (3 and 4) had improved estimates by the V_d-aided GLLS as compared with the original GLLS. The BMC-aided GLLS provided slightly higher estimates of K_1 and V_d in contrast to the results achieved by the BMC-V_d-aided GLLS, which was consistent with our findings from the simulation data.

IV. DISCUSSION

We recently proposed enhanced GLLS algorithms with improved immunity to noise and evaluated them with simulated TTACs with Gaussian noise added [9]. The BMC-V_d-aided GLLS method was concluded to provide the least bias and better reliably for the simulated TTACs. While this study clearly identified the potential of these techniques, the simulated TTACs did not necessarily completely reflect the noise, correlations,

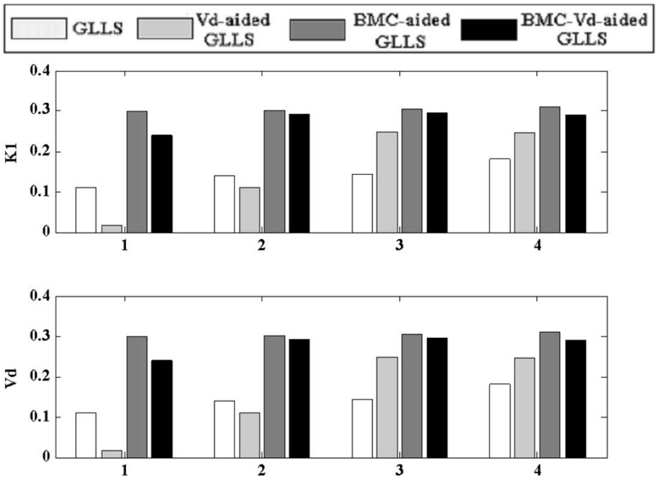

Fig. 8. Mean values of K_1 and $V_{\rm d}$ across the voxels of manually defined ROI for frontal cortex in the experimental studies.

resolution effects introduced by the imaging, and reconstruction process in voxel TTACs used for generating parametric images. A systematic investigation, as carried out in this study, using realistically simulated imaging data and incorporating these factors was thus warranted.

The Monte Carlo simulation has been validated by obtaining SPECT data for a line source filled with ^{123}I in [19]. The limited spatial resolution (12-mm FWHM for the simulated system) of SPECT leads to profound PVE degrading the quantitation of estimated parameters even for the simulated data without noise (approximately -20% for K_1 and $V_{\rm d}$ in Fig. 3). PVE correction usually requires coregistered high-resolution anatomical images or knowledge of the point spread function. As one factor contributing to PVE, the distance-dependent spatial resolution caused by collimators in SPECT systems can be partially compensated in iterative reconstruction with resolution recovery. Despite achieving biases close to 0% for the noise-free simulation data (Fig. 5), positive biases of K_1 and $V_{\rm d}$ were still observed for the cerebellum and thalamus. This implies that the reconstruction-based resolution recovery in our investigation did not provide optimal resolution recovery for all the regions with noisy data. Other PVE correction techniques may provide improved recovery, but are beyond the scope of this study. However, resolution recovery exhibited some positive attributes. For example, the noise in the resolution recovery parametric image is reduced (Fig. 6), and as noted before, the computation time for the BMC methods is reduced with resolution recovery, compared to the BMC analyses without resolution recovery. Thus, overall, incorporation of resolution recovery is worthwhile, even though it can result in positive bias in $V_{\rm d}$.

The binding potential (BP) functional parameter is often used in the kinetic analysis of receptor studies. However, the high level of noise in SPECT imaging can lead to low reliability of $\mathrm{BP} = k_3/k_4$ parametric images due to the microrate constants (k_3 and k_4) being very sensitive to noise variation. In contrast, volume of distribution ($V_{\rm d}$), which also describes the functional capability of receptors, has relatively high reliability compared with BP. One purpose of this study was to derive multiple parametric images simultaneously. Thus, the influx rate of K_1, which is related to the tracer transport rate across capillaries and into the cell, and $V_{\rm d}$ were used as the parameters of interests.

The results demonstrate that the simple constraint in the parametric domain of a prior $V_{\rm d}$ ($V_{\rm d}$-aided GLLS) was unable to improve the parameter estimation reliability. It gives rise to physiologically meaningless fits with negative estimates of rate constants. This finding is generally in line with our previous results, except that the deterioration of the reliability with noise was more pronounced for the voxel TTACs used in this study, compared to the simulated TTACs used in the previous study. In contrast, the incorporation of the BMC technique substantially enhanced the performance of $V_{\rm d}$-aided GLLS, again demonstrating a similar trend to that seen in our previous study.

The BMC method is a type of Monte Carlo method that can generate synthetic data from observed data. In molecular imaging, the BMC technique has been applied to analyze statistical properties and noise effects [20], [21]. The post-reconstruction BMC method has been validated to provide a similar assessment and measure of accuracy and reliability of parameter estimates as the traditional Monte Carlo technique for the ROI-based TTACs [8]. For the resolution-recovered simulation data, similar results were obtained as compared with our recent work [9]. The BMC-aided GLLS achieved less bias for K_1 (by about 6%) than the BMC-$V_{\rm d}$-aided GLLS, while the BMC-$V_{\rm d}$-aided GLLS achieved about 14% less bias for $V_{\rm d}$ for the cerebellum and bias in the thalamus was reduced by approximately 31%.

Distinct findings were obtained for the lower SNR simulation data without resolution recovery. The BMC-aided GLLS not only achieved better estimates of K_1 but also obtained slightly better estimates of $V_{\rm d}$, as shown in Table III, because the quantification loss of PVE is partially compensated by the overestimated $V_{\rm d}$ by the BMC-aided GLLS for the frontal cortex [Fig. 3(b)]. In terms of the kinetics of the studied compartmental model (Fig. 1), K_1 is related to the curve shape early on in the study, while $V_{\rm d}$ is more related to curve trends at a late period. The results of underestimated K_1 and overestimated $V_{\rm d}$ by the BMC-aided GLLS imply that successful fits of the BMC-aided GLLS favored BMC curves resampled from the noisy curves that exhibited a relative decrease in the early period and increase at late time points. This gave rise to higher $V_{\rm d}$ estimates and lower K_1 values compared to the reference parameters.

The EMSE measure is capable of evaluating the overall performance of parameter estimation combining the estimated bias and variance into a single measure. However, EMSE masks the relative contributions of bias and reliability, which provide additional insight into the comparative performance of the approaches. For example, the quite low CV for the enhanced methods is not apparent from the EMSE, which in this case is predominantly governed by the bias. Thus, percentage bias and CV were used in the investigation to provide a more complete comparison between the techniques, despite the attraction of a single parameter (EMSE) comparison.

For the GLLS fitting, the running time of generating parametric images was dependent on the total number of BMC curves that had to be generated and fitted to get the required number of successful fits (in this case ten). This is why the computational cost associated with the BMC methods is increasing when imaging data tends to be noisier, i.e., lower SNR. Interestingly, running time for the BMC methods with resolution recovery was reduced compared to the data without resolution recovery. This is likely due to the reduced noise in the resolution recovery reconstructions. Further investigation to decrease running time is required for the clinical application of these methods.

V. CONCLUSION

The computer simulation and experimental data show that the enhanced GLLS methods with BMC technique are efficient in generating reliable parametric images for challenging functional imaging. For high SNR imaging data, the BMC-aided GLLS provides best estimates of K_1, while the BMC-V_{d}-aided GLLS provides best estimates of V_{d}. The BMC-aided GLLS is more suitable in the application dealing with low SNR imaging data at the expense of overestimation of V_{d} and increased computation time. Resolution recovery reduced the underestimation due to bias and noise in the parametric image, but exacerbated the overestimation of V_{d} with the BMC methods. In addition, it reduced the computation time for the BMC methods.

REFERENCES

[1] S.-C. Huang, M. E. Phelps, E. J. Hoffman, K. Sideris, C. Selin, and D. E. Kuhl, “Noninvasive determination of local cerebral metabolic rate of glucose in man,” *Amer. J. Physiol.*, vol. 238, pp. E69–E82, 1980.

[2] C. Patlak and R. G. Blasberg, “Graphical evaluation of blood-to-brain transfer constants from multiple-time uptake data. Generalizations,” *J. Cereb. Blood Flow Metab.*, vol. 5, pp. 584–590, 1985.

[3] J. Logan, N. D. Volkow, J. S. Fowler, G.-J. Wang, S. L. Dewey, R. Macgregor, D. Schlyer, S. J. Gatley, N. Pappas, P. King, R. Hitzemann, and S. Vitkun, “Effects of blood flow on [^{11}C] Raclopride binding in the brain: Model simulations and kinetic analysis of PET data,” *J. Cereb. Blood Flow Metab.*, vol. 14, pp. 995–1010, 1994.

[4] D. Feng, Z. Wang, and S.-C. Huang, “A study on statistically reliable and computationally efficient algorithms for generating local cerebral blood flow parametric image with positron emission tomography,” *IEEE Trans. Med. Imag.*, vol. 12, no. 2, pp. 182–188, Jun. 1993.

[5] D. Feng, S.-C. Huang, Z. Wang, and D. Ho, “An unbiased parametric imaging algorithm for nonuniformly sampled biomedical system parameter estimation,” *IEEE Trans. Med. Imag.*, vol. 15, no. 4, pp. 512–518, Aug. 1996.

[6] K. Chen, M. Lawson, E. Reiman, A. Cooper, D. Feng, S.-C. Huang, D. Bandy, D. Ho, L.-S. Yun, and A. Palant, “Generalized linear least squares method for fast generation of myocardial blood flow parametric images with N-13 ammonia PET,” *IEEE Trans. Med. Imag.*, vol. 17, no. 2, pp. 236–243, Apr. 1998.

[7] H.-C. Choi, S. Chen, D. Feng, and K. P. Wong, “Fast parametric imaging algorithm for dual-input biomedical system parameter estimation,” *Comput. Methods Programs Biomed.*, vol. 81, pp. 49–55, 2006.

[8] L. Wen, S. Eberl, K. P. Wong, D. Feng, and J. Bai, “Effect of reconstruction and filtering on kinetic parameter estimation bias and reliability for dynamic SPECT: A simulation study,” *IEEE Trans. Nucl. Sci.*, vol. 52, no. 1, pp. 69–78, Feb. 2005.

[9] L. Wen, S. Eberl, H.-C. Choi, D. Feng, and M. Fulham, “Enhanced parameter estimation methods for noisy SPECT data,” *Comput. Methods Programs Biomed.*, vol. 89, pp. 102–111, 2008.

[10] D. Feng, D. Ho, K. Chen, L.-C. Wu, J.-K. Wang, R.-S. Liu, and S.-H. Yeh, “An evaluation of the algorithms for determining local cerebral metabolic rates of glucose using positron emission tomography dynamic data,” *IEEE Trans. Med. Imag.*, vol. 14, no. 4, pp. 697–710, Dec. 1995.

[11] H.-C. Choi, L. Wen, S. Eberl, and D. Feng, “Methods for improving reliability of GLLS for parametric image generation,” presented at the *6th IFAC Symp. Modelling Contr. Biomed. Syst.*, Reims, France, 2006.

[12] W. H. Press, S. A. Teukolsky, W. T. Vetterling, and B. P. Flannery, *Numerical Recipes in C: The Art of Scientific Computing*, 2nd ed. Cambridge, U.K.: Cambridge Univ. Press, 1992.

[13] I. G. Zubal, C. R. Harrell, E. O. Smith, Z. Rattner, G. Gindi, and P. B. Hoffer, “Computerized 3-dimensional segmented human anatomy,” *Med. Phys.*, vol. 21, pp. 299–302, 1994.

[14] T. K. Lewellen, R. L. Harrison, and S. Vannoy, “The Simset program,” in *Monte Carlo Calculations in Nuclear Medicine, Medical Science Series*, M. Liungberg, S. E. Strand, and M. A. King, Eds. Bristol, PA: Institute of Physics Publishing, 1998, pp. 77–92.

[15] M. Kassiou, S. Eberl, S. R. Meikle, A. Birrell, C. Constable, M. J. Fulham, D. F. Wong, and J. L. Musachio, “In vivo imaging of nicotinic receptor upregulation following chronic (−)-nicotine treatment in baboon using SPECT,” *Nuclear Med. Biol.*, vol. 28, pp. 165–175, 2001.

[16] S. R. Meikle, B. F. Hutton, and D. L. Bailey, “A transmission-dependent method for scatter correction in SPECT,” *J. Nuclear Med.*, vol. 35, pp. 360–367, 1994.

[17] H. Iida, Y. Narita, H. Kado, A. Kashikura, S. Sugawara, Y. Shoji, T. Kinoshita, T. Ogawa, and S. Eberl, “Effects of scatter and attenuation correction on quantitative assessment of regional cerebral blood flow with SPECT,” *J. Nuclear Med.*, vol. 39, pp. 181–189, 1998.

[18] H. M. Hudson and R. S. Larkin, “Accelerated image reconstruction using ordered subsets of projection data,” *IEEE Trans. Med. Imag.*, vol. 13, no. 4, pp. 601–609, Dec. 1994.

[19] L. Wen, S. Eberl, D. Feng, W. Cai, and J. Bai, “Fast and reliable estimation of multiple parametric images using an integrated method for dynamic SPECT,” *IEEE Trans. Med. Imag.*, vol. 26, no. 2, pp. 179–189, Feb. 2007.

[20] I. Buvat, “A non-parametric bootstrap approach for analysing the statistical properties of SPECT and PET images,” *Phys. Med. Biol.*, vol. 47, pp. 1761–1775, 2002.

[21] M. Dahlbom, “Estimation of image noise in PET using bootstrap method,” *IEEE Trans. Nucl. Sci.*, vol. 49, no. 5, pp. 2062–2066, Oct. 2003.

Lingfeng Wen (S'02–M'04) received the B.E. and Ph.D. degrees in biomedical engineering from the Tsinghua University, Beijing, China, in 1998 and 2004, respectively.

He is currently a Principal Hospital Scientist in the Department of PET and Nuclear Medicine, Royal Prince Alfred Hospital, Sydney, NSW, Australia. He was a Postdoctoral Research Fellow in the School of Information Technologies, University of Sydney, Sydney, where he is currently an Honorary Research Associate. During 2008, he was a Visiting Researcher in the Department of Electronic and Information Engineering, Hong Kong Polytechnic University. His current research interests include kinetic analysis, modeling and simulation, computer-aided diagnosis, image processing, and analysis of multimodality imaging data.

Dr. Wen is a member of the International Federation of Automatic Control (IFAC) Technical Committee on Biological and Medical Systems.

Stefan Eberl (M'97) received the B.E. (Hons.) degree in electrical engineering from New South Wales (NSW) Institute of Technology, Sydney, NSW, Australia, in 1982, and the M.S. degree in physics and Ph.D. degree in biomedical engineering from the University of New South Wales, Sydney, in 1987 and 2001, respectively.

He is currently a Principal Hospital Scientist in the Department of PET and Nuclear Medicine, Royal Prince Alfred Hospital, Sydney, and an Adjunct Associate Professor at the School of Information Technologies, University of Sydney, Sydney. His current research interests include physiological parameter estimation from functional imaging, image registration, and optimizing use of the combination of functional/anatomic data.

Michael J. Fulham received the M.B.B.S. (Hons.) degree from the University of New South Wales, Sydney, NSW, Australia, in 1979.

He was engaged in the training of internal medicine and neurology at Royal Prince Alfred (RPA) Hospital, Sydney. From 1988 to 1993, he was working in positron emission tomography (PET) and magnetic resonance (MR) spectroscopy in the Neuroimaging Branch of National Institute of Neurological and Communicative Disorders and Stroke (NINCDS), National Institutes of Health, Bethesda, MD. Since 1993, he has been a Neurologist at RPA Sydney, where he was placed in charge of the PET Program. He is currently the Director of the PET Program at RPA and the first Clinical Director of medical imaging services for the Sydney South West Area Health Services (SSWAHS). The PET program at RPA is the largest in the country and scans close to 6000 patients each year. The PET program has its own medical cyclotron and 2 PET-CT scanners including an extended field of view 64-slice PET-CT scanner with an active research program that utilizes a local baboon colony for preclinical functional imaging experiments.

(David) Dagan Feng (S'88–M'88–SM'94–F'03) received the M.E. degree in electrical engineering and computing science from Shanghai Jiao Tong University, Shanghai, China, in 1982, the M.S. degree in biocybernetics and the Ph.D. degree in computer science from the University of California, Los Angeles, in 1985 and 1988, respectively.

He is the Founder and the Director of the Biomedical and Multimedia Information Technology (BMIT) Research Group and a Professor in the School of Information Technologies, University of Sydney, Sydney, NSW, Australia; the Chair Professor of Information Technology, Hong Kong Polytechnic University; an Advisory Professor and the Chief Scientist of the Med-X Research Institute, Shanghai Jiao Tong University. He has authored or coauthored over 500 scholarly research papers, pioneered several new research directions, and made a number of landmark contributions in his field.

Prof. Feng is also a fellow of the Australian Academy of Technological Sciences and Engineering, Australian Computer Society (ACS), Hong Kong Institution of Engineers (HKIE), and Institution of Engineering and Technology (IET).

Jing Bai (M'87–SM'92–F'01) received the M.S. and Ph.D. degrees from Drexel University, Philadelphia, PA, in 1983 and 1985, respectively.

From 1985 to 1987, she was a Research Associate and an Assistant Professor with the Biomedical Engineering and Science Institute, Drexel University. In 1988, she was an Associate Professor in the Department of Biomedical Engineering, Tsinghua University, Beijing, China, where she became a Professor in 1991 and the Cheung Kong Chair Professor in 2000. Her current research interests include optical molecular imaging, mathematical modeling and simulation of cardiovascular system, optimization of cardiac assist devices, medical ultrasound, telemedicine, and home health care network and home monitoring devices. She has authored or coauthored four books and over 200 journal papers.

Prof. Bai became an Associate Editor for the IEEE TRANSACTIONS ON INFORMATION TECHNOLOGY AND BIOMEDICS in 1997.